Electronic Supplementary Information for

Tungsten Boride: a 2D Multiple Dirac Semimetal for

Hydrogen Evolution Reaction

Aizhu Wang[1,2], Lei Shen[3], Mingwen Zhao[4]*, Junru Wang [4], Weifeng Li[4], Weijia Zhou[1],

Yuanping Feng[5]*, and Hong Liu[1,6]*

[1]*Institute for Advanced Interdisciplinary Research, University of Jinan, Jinan, Shandong, 250022, China*

[2]*Department of Electrical and Computer Engineering and Department of Physics, National University of Singapore, Singapore, 117579, Singapore*

[3]*Department of Mechanical Engineering, Engineering Science Programme, Faculty of Engineering, National University of Singapore, Singapore, 117575, Singapore*

[4]*School of Physics and State Key Laboratory of Crystal Materials, Shandong University, Jinan 250100, Shandong, China*

[5]*Department of Physics & Centre for Advanced Two-dimensional Materials, National University of Singapore, Singapore, 117542, Singapore*

[6]*State Key Laboratory of Crystal Materials, Shandong University, Jinan, 250100, Shandong, China*

*Correspondences:

zmw@sdu.edu.cn (M. Z.)

phyfyp@nus.edu.sg (Y. F.)

hongliu@sdu.edu.cn (H. L.)

Part I The band structures of tungsten diboride

  Figure S1(a) gives the top view and side view, respectively, of the tungsten diboride configuration, where the triangle lattice W atoms are located above the center of the honeycomb graphene-like boron lattice from the top view, form a "sandwich". The bond lengths are 1.746 Å, 2.513 Å and 3.025 Å for B-B, W-B and W-W, respectively. Values of a = 3.025 Å and c = 3.329 Å is calculated for a hexagonal unit cell, fitting well with the experiment data (a = 3.020 Å and c = 3.050 Å). Clearly, the bulk materials are metallic with several bands across the Fermi level, as shown in the electronic band structure (Figure S1(b)). This is in good agreement with good electron conductivity of the tungsten diboride found in experiments[1].
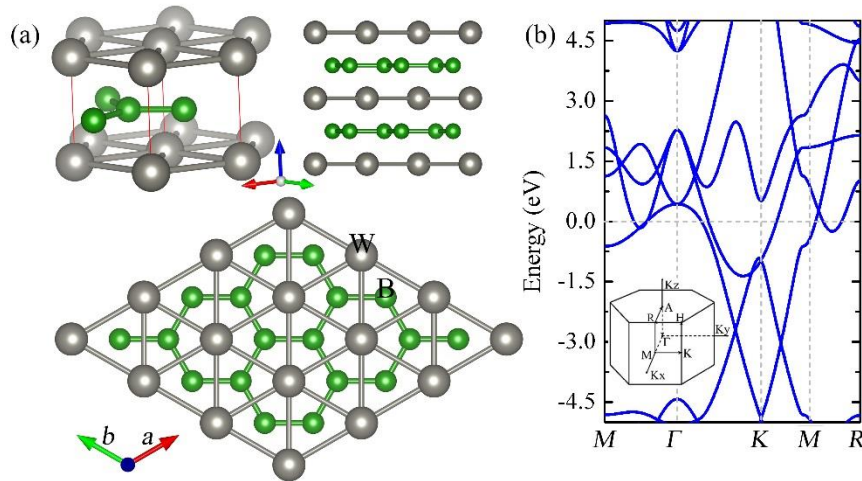

Figure S1 (a) Schematic illustration of fabrication of WB$_2$ (P6/mmm, number 191) crystal. The unit cell is indicated by the red line. (b) The calculated band structures based on PBE calculations were also listed here. The energy at the Fermi level was set to zero.
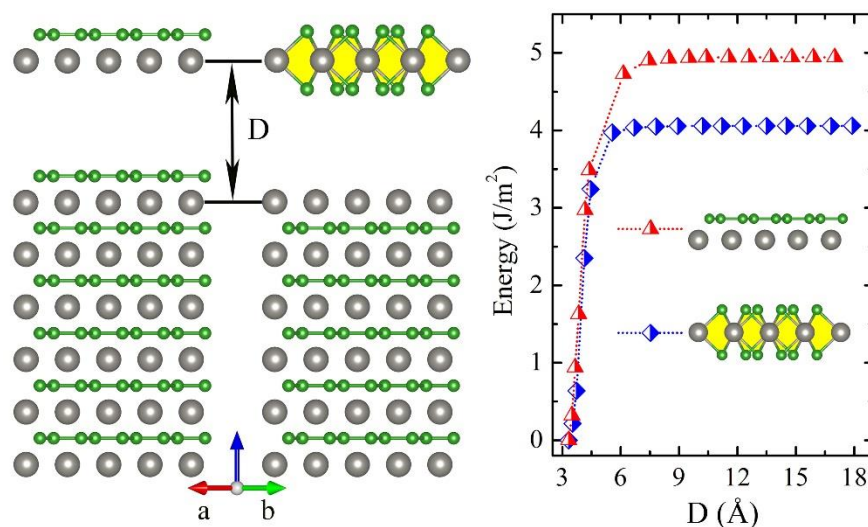
Figure S2 (a) Schematic representation of the exfoliation process of WB_2 monolayer and WB_4 monolayer. (b) Energy increase E as a function of interlayer distance (D).

Then, the possibility of producing WB_4 monolayer using a mechanical exfoliation strategy was confirmed (Figure 2S). The cleavage energy E_{cl} is defined as the minimum energy required to exfoliate a monolayer from bulk. We used a seven-slab model to mimic a bulk material and calculated the energy increase as a WB_4 monolayer is exfoliated from the slab. A vacuum layer at least 15 Å was incorporated into the seven-layer slab to avoid the artificial interaction between two neighboring slabs. Figure S2 gives the variation of energy (and its derivative) as a function of the interlayer distance (D) between the top most monolayer and the remnant layers, which was fixed during the exfoliation process. The calculated cleavage energy E_{cl} of WB_4 is about 4.06 J m^{-2}. The cleavage strength (χ) was further obtained from the derivative of energy with respect to the distance, which is about 2.66 GPa. It is noteworthy that the calculated cleavage energy of WB_4 is smaller than that of WB_2 suggesting high plausibility to extract the WB_4 monolayer from the bulk in experiments.

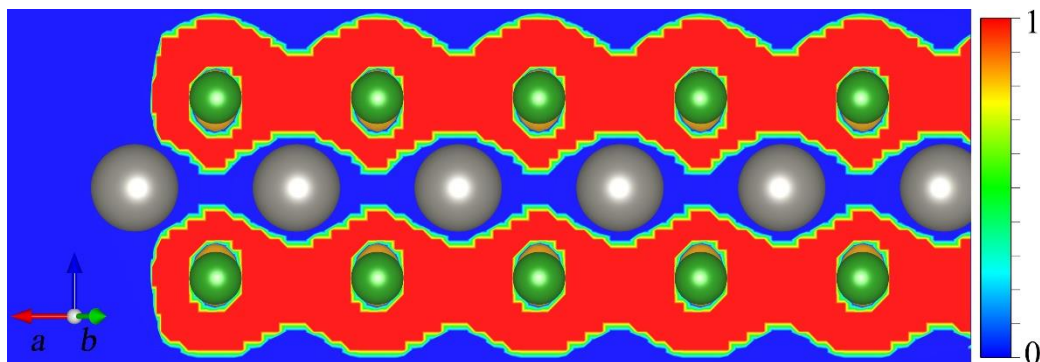# Part II The thermodynamic stability and electronical properties of WB₄

Figure S3 (Color online). The electron localization function (ELF) profiles on the plane perpendicular to the basal plane of the monolayers with an isovalue of 0.4 Å⁻³

The structure of WB₄ can be viewed as an interconnected, sandwich-like configuration comprising W framework-inserted borophene subunits. The electron localization function (ELF)[2] profile of the WB₄ monolayer indicates that B atoms are chemically bonded to the triangle W lattice, while the covalent like B-B bonds are preserved, as shown in Figure S3. Obviously, the metal bonds have longer bond lengths so that metallic like W-B bonds are weaker, meanwhile, electron density redistribution takes place around W and B atoms, which facilitates the protection of semimetal phase and HER performance of the WB₄ framework.
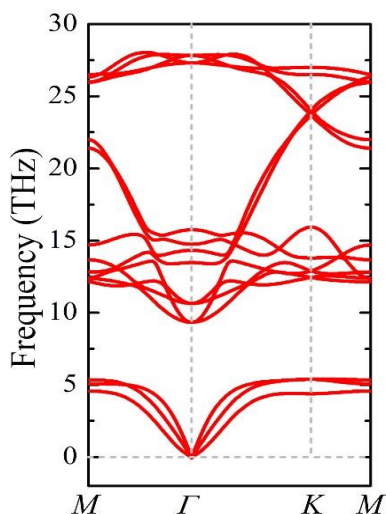
Figure S4 (Color online) Phonon spectrum of WB$_4$ along the high symmetric points in BZ. Clearly, the phonon spectrum is free from imaginary frequencies, suggesting that the WB$_4$ framework is kinetically stable. The optical and acoustical branches are well separated in the spectrum. Two acoustical branches have linear dispersion relationships near the center of BZ (Γ point).
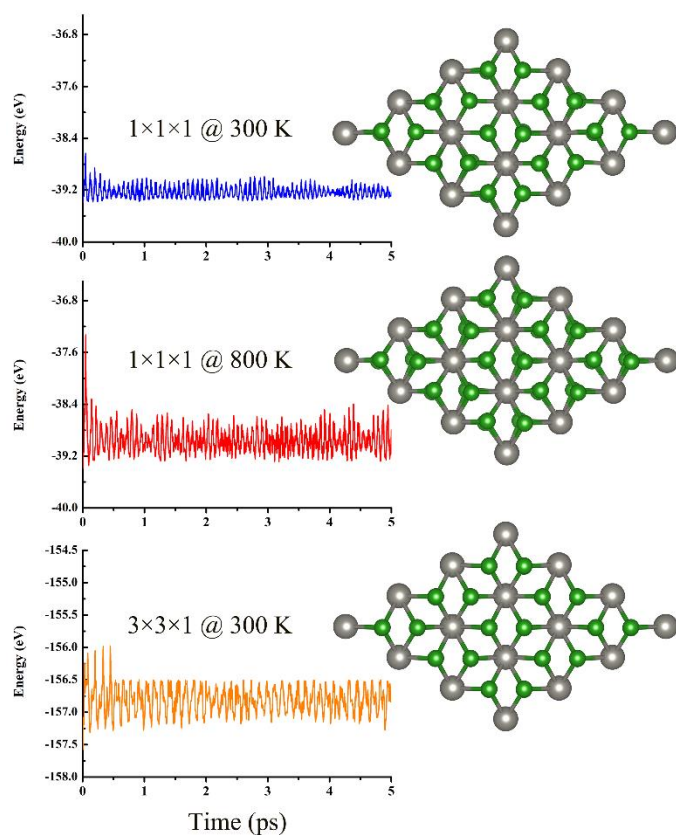

Figure S5 (Color online). The fluctuations of energy (with different models) as functions of the molecular dynamic (MD) simulation step at 300 K and 800 K. Our MD simulations clearly indicate that geometry of WB$_4$ remains unchanged in addition to small fluctuations of the temperature and the total energy with the passage of time. Although the time scale is short, our MD results imply that the WB$_4$ framework is stable at room temperature (300 K), but no longer unstable at high temperature (800 K).
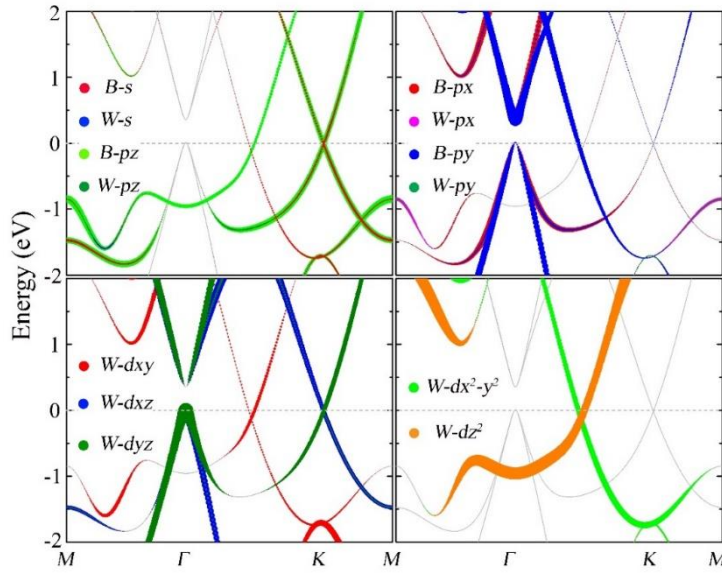
Figure S6. (Color online) Orbital-resolved band structures around Fermi level based on PBE calculations. The size of colorful dots is proportion to the contribution of the different orbitals on the wave function. The energy at the Fermi level was set to zero.
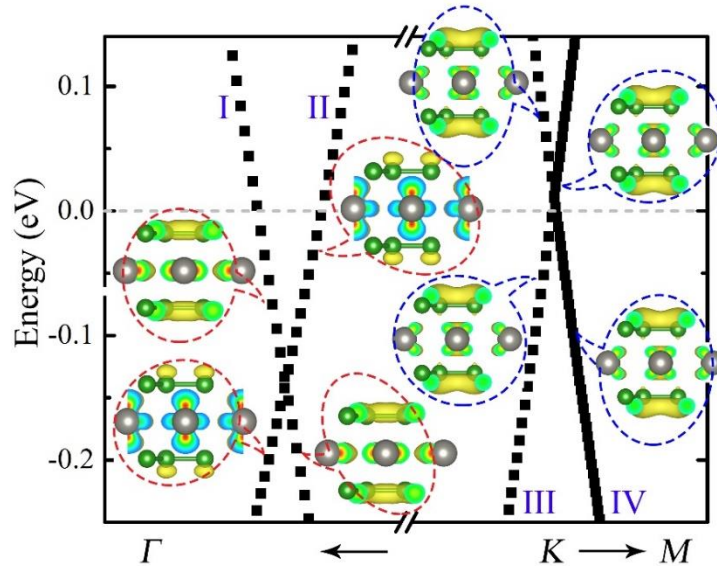

Figure S7. Charge density distributions near the Fermi level, both Dirac cone (cone ii and cone iii) are from d orbitals of W and p orbitals of B atoms. Cone iii, made up of bands III and IV, is isotropic with a high symmetry, while, cone ii, made up of bands I and II, is anisotropic with a lower symmetry. The energy at the Fermi level was set to zero.
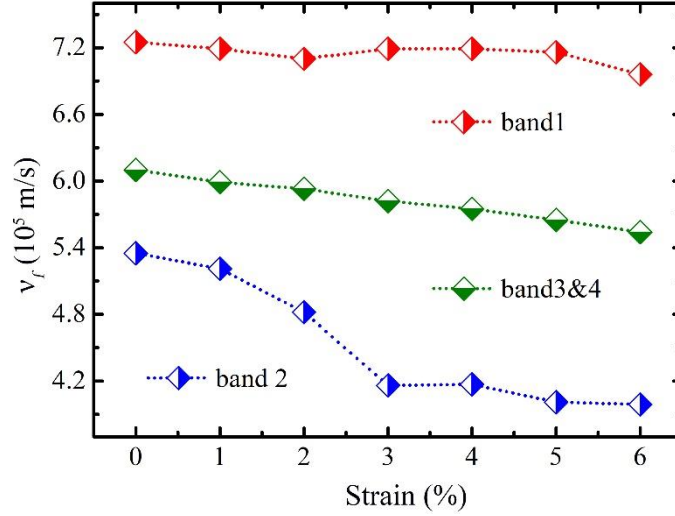
Figure S8 Fermi velocity evolutions of Dirac bands in the 2D WB$_4$ lattice with external stretching strain along the *xy*-direction.

The charge carriers in these linear bands will behave as massless Dirac fermions. The Fermi velocity (v_f) of the WB$_4$ lattice can be tested by fitting those Dirac bands at $k = K + q$ to the expression of $\upsilon_f = E(q)/\hbar |q|$. The Fermi velocities are 0.72×10^6 m/s (band I), 0.54×10^6 m/s (band II) and 0.61×10^6 m/s (bands III and IV), respectively. These values are approximately 83.72%, 62.72% and 70.85% of that of graphene (0.86×10^6 m/s) from the present calculations. Apart from the equalitarian state, we also investigated the robustness of semimetal states and Fermi velocities of the WB$_4$ monolayer under finite biaxial strain (-3% ~ 6%). Interestingly, the electronic structure of the WB$_4$ lattice responds differently to compressive (negative sign) and tensile (positive sign) strains as shown in **Figure 3**. The semimetal feature is robust against the stretching along the *xy*-direction, but gradually converts into metal characteristic with abundant states around E_f under the compressional condition. As for those semimetal states, thanks for the configure symmetry and the out-of-plain coupling of orbitals (p_z and d_{xz}/d_{yz}), the Dirac cone iii remains intact, but with a linear decreasing v_f from 0.61×10^6 m/s to 0.55×10^6 m/s. Affected by Γ point, the v_f of band I almost keeps a constant, however, the value of band II has a sharp drop as shown in **Figure S8**.
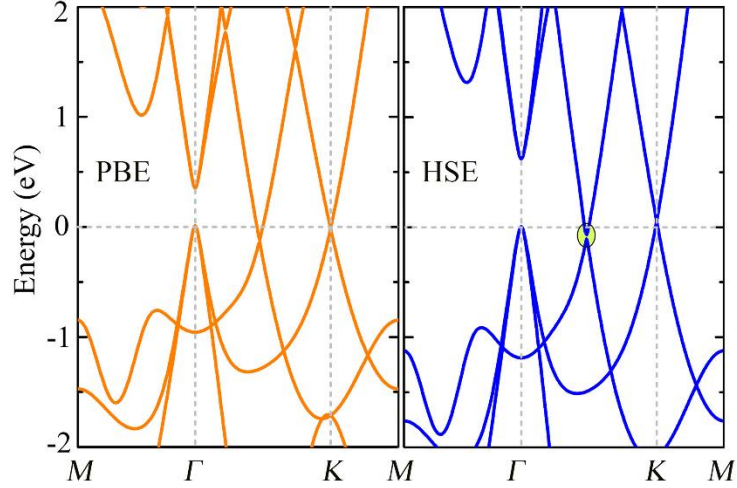
Figure S9 (Color online) Electronic band lines of WB$_4$ in proximity of the Fermi level (set to zero) along the high symmetric points in BZ obtain from DFT calculations within the PBE functional (left column) and HSE06 functional (right column), respectively. The energy at the Fermi level is set to zero.

The hybrid functional (HSE06) was adopted to detect the semi-metallic features of the WB$_4$ lattice. In addition to the faint shift above the E_f, the cone I remain intact with $v_f = 0.73 \times 10^6$ m/s as shown in the right column of **Figure S9**. Though the cone II still locates below the E_f, a small gap (39 meV) comes out due to HSE correction. The orbital-resolved band structures based on HSE06 function verify that both the Dirac cone I and pseudo Dirac cone II have the same origins just as mentioned above PBE calculations. Thus, the WB$_4$ will has an excellent electronic transport property due to the existence of the cone I as well as the pseudo Dirac cone II, opening a brand-new avenue for the potential applications of HER performance.

Part III The hydrogen evolution reaction calculations

Here, we adopt a (2×2) WB$_4$ 2D supercell to study it's HER performance. On the basal plane of WB$_4$, there are three potential hydrogen adsorption sites, *i.e.*, W top site, B top site and the bridge site of B-B bond. The hydrogen adsorption energies on these sites are calculated and summarized in Table 1. The bridge site of B-B bond is the most stable adsorption site with ΔE_H = -0.34 eV. The adsorption of hydrogen is much weak for the B top site (-0.17 eV) and is unfavorable for the W top sites (positive values). Therefore, we will only focus on bridge site hereafter.

Table S1. Hydrogen adsorption energies on potential adsorption sites of WB$_4$ and the height of the hydrogen atom above the surface.

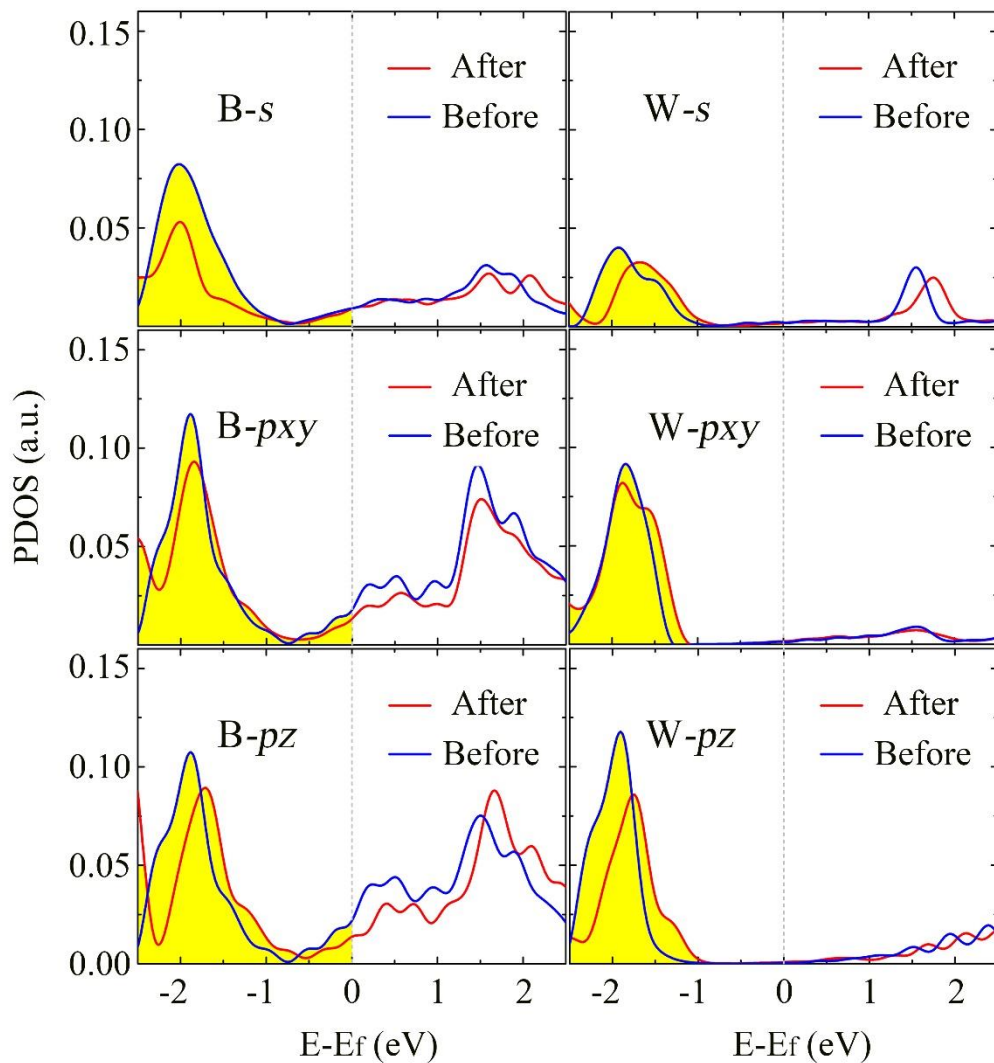| Adsorption site		Adsorption energy (eV)	Δz (Å)
W top sites	1	5.56	0.27
	2	1.51	0.67
	3	1.51	0.65
B top site		-0.11	1.28
Bridge site of B-B bond		-0.31	1.01

Figure S10 (Color online) The projected density of states (PDOS) for the *s*- and *p*-orbitals of B and W atom under the condition with (after) and without (before) hydrogen adsorption. The energy at the Fermi level was set to zero.
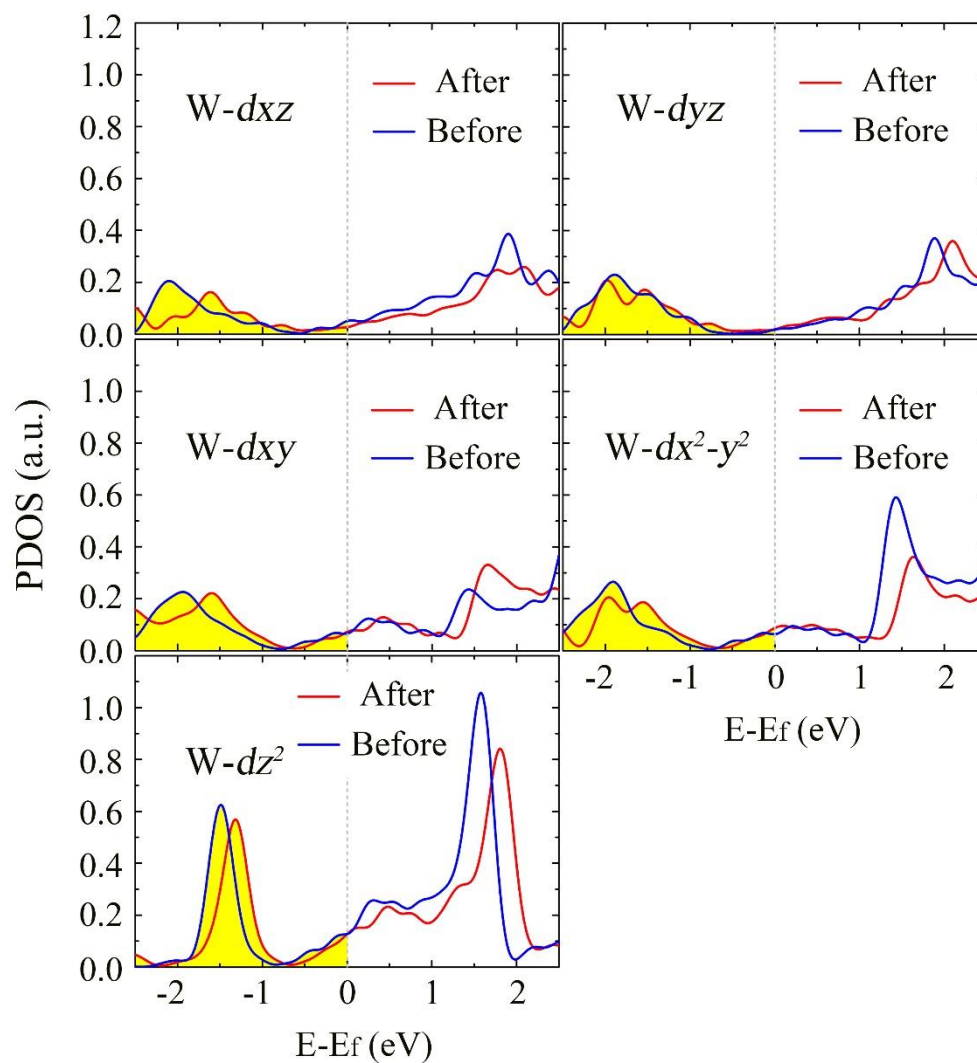
Figure S11 (Color online) The projected density of states (PDOS) for the *d*-orbitals of W atom under the condition with (after) and without (before) hydrogen adsorption. The energy at the Fermi level was set to zero.
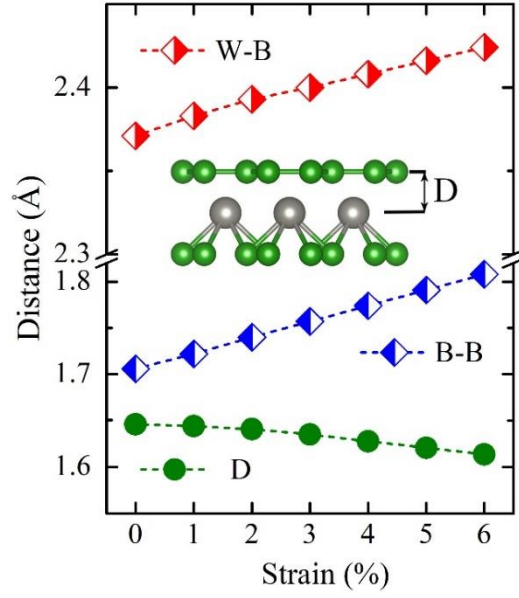
Figure S12 (Color online) The evolutions of bonds. It can be clearly seen that the perpendicular distance between B and W decreases with the increase of lattice constant. And the hybridization between p-orbitals of B atoms and d-orbitals of W will change accordingly.
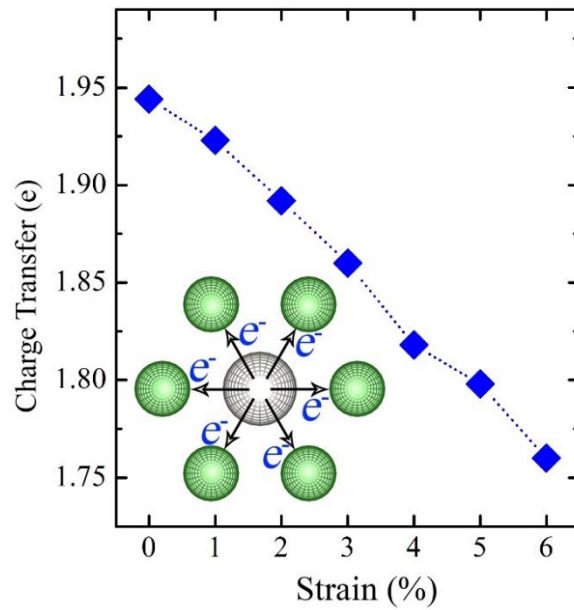

Figure S13 (Color online) The evolutions of charge transfer from W atom to the surrounding B atoms in WB_4 nanosheet without hydrogen adsorption.
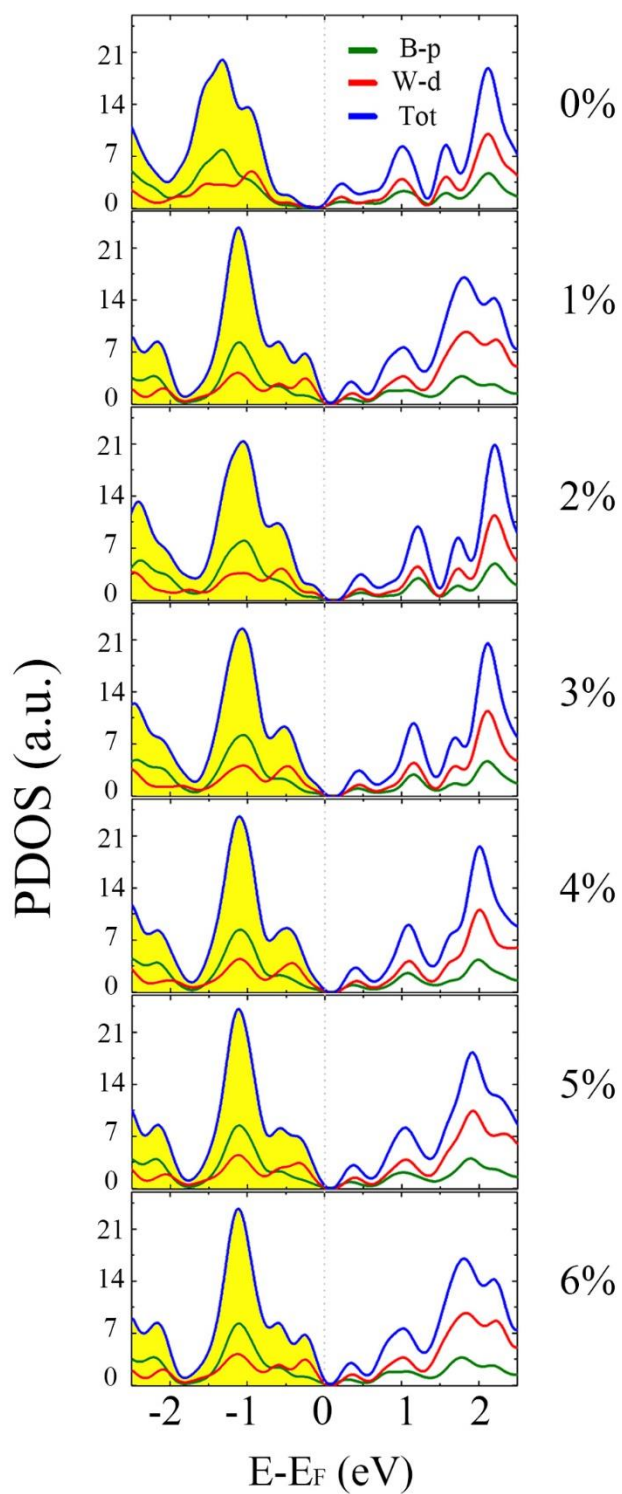
Figure S14 (Color online) The evolutions of the projected density of states (PDOS) for B and W atoms. The energy at the Fermi level was set to zero.
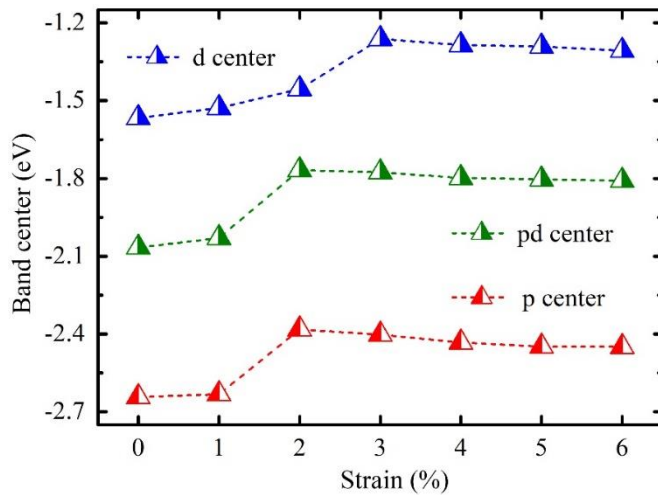
Figure S15 (Color online) The evolutions of the band center. The energy at the Fermi level was set to zero. In the process of stretching, the *d* band center plays a leading role for the evolutions of catalyst activity.
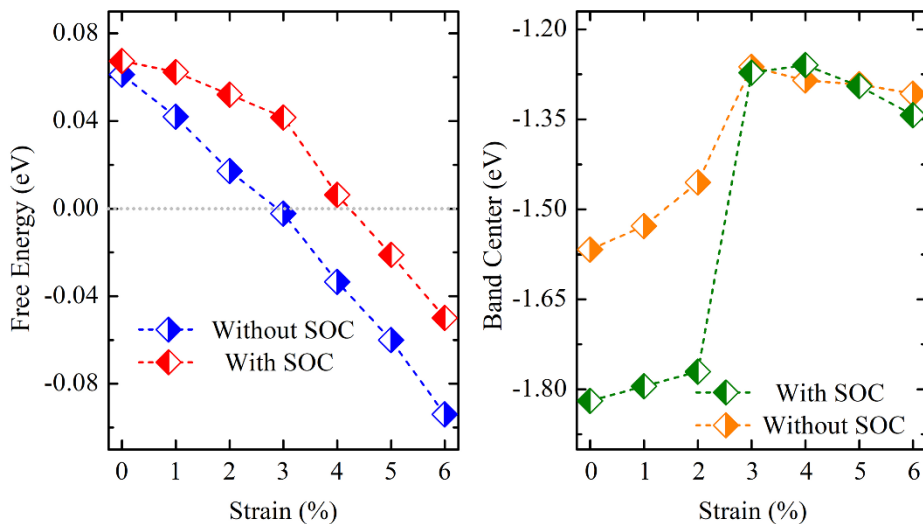

Figure S16 (Color online) The evolutions of Gibbs free energy and *d*-band center (with and without SOC interaction). The energy at the Fermi level was set to zero.

The surface Pourbaix diagrams of the equalitarian (0%) and strained (3%) states are constructed by plotting the thermodynamically most stable surface state under the relevant U_{SHE} and pH values. In our model, we assumed that the oxidation of water to OH* and O* on WB_4 lattice occurred through the following steps as suggested in ref [3]:

$$H_2O + * \rightarrow OH* + H^+ + e^-$$
$$OH* \rightarrow O* + H^+ + e^- \tag{1}$$
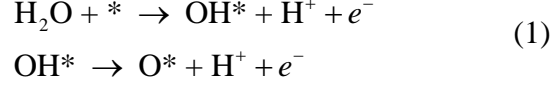
Under standard conditions, the free energy of $H^+ + e^-$ is equal to $1/2$ H_2. Therefor, the above equations can be rewritten as the following:

$$H_2O + * \rightarrow OH* + \frac{1}{2}H_2 \qquad \Delta G_1^0$$
$$OH* \rightarrow O* + \frac{1}{2}H_2 \qquad \Delta G_2^0 \tag{2}$$
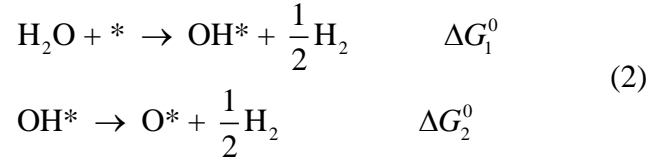
The Gibbs free energyies of ΔG_1^0 and ΔG_2^0 are obtained by

$$\Delta G^0 = \Delta E + \Delta E_{ZPE} - T\Delta S \tag{3}$$

where ΔE is the energy difference from with and without adsorbtion. The values from E_{ZPE}-$T\Delta S$ are calcualted on the basis of value from Table 1 of ref[4].

Equation (1) is deoendent on the pH and potential U through the chemical potential of $H^+ + e^-$, while, equation (2) is not. To include the effects of pH and potential U, equation (3) can be rewritten as equation (4):

$$\Delta G_1 = \Delta G_1^0 - eU_{SHE} - k_bT \ln 10 \times pH$$
$$\Delta G_2 = \Delta G_2^0 - eU_{SHE} - k_bT \ln 10 \times pH \tag{4}$$

The free enrgy change of OH* and O* termination can be express by

$$\Delta G_{OH^*} = \Delta G_1$$
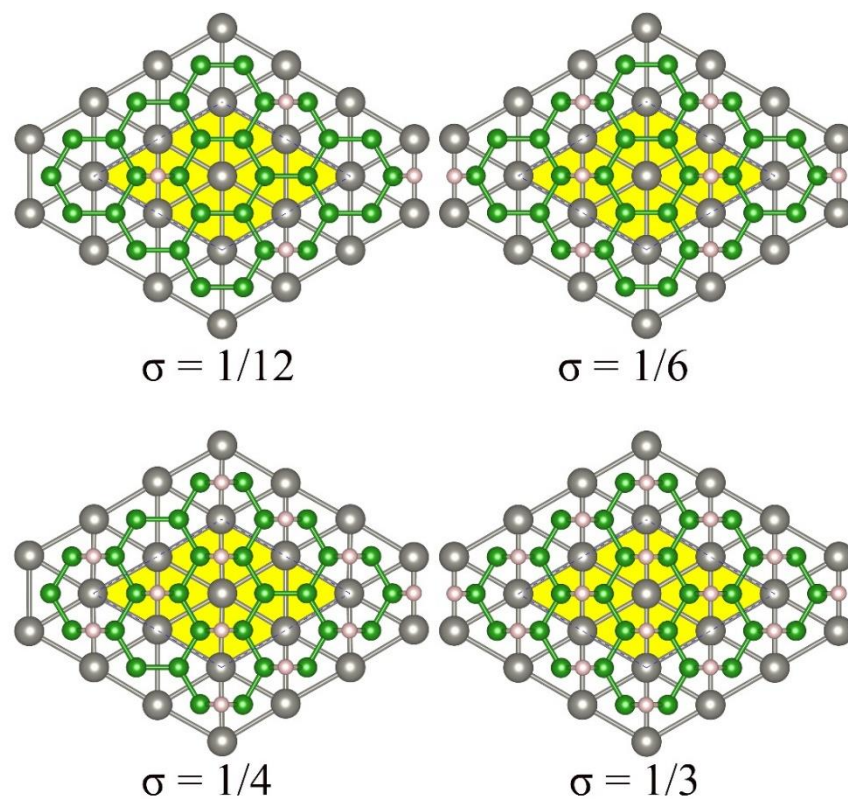$$\Delta G_{O^*} = \Delta G_1 + \Delta G_2$$

Figure S17 Schematic illustration of stable adsorption states with different hydrogen covering. The unit cell is indicated by the yellow shaded area.

References

1. H. Woods, F. Wawner and B. G. Fox, *Science*, 1966, **151**, 75-75.

2. A. Savin, O. Jepsen, J. Flad, O. K. Andersen, H. Preuss and H. G. von Schnering, *Angew. Chem. Inter. Ed.*, 1992, **31**, 187-188.

3. H. A. Hansen, J. Rossmeisl and J. K. Nørskov, *Phys. Chem. Chem. Phys.*, 2008, **10**, 3722-3730.

4. H. Xu, D. Cheng, D. Cao and X. C. Zeng, *Nat Catal*, 2018, **10**, 339-348.